Supplementary Information (SI) for Journal of Materials Chemistry A.

Supporting Information for:

Electron donation of Violet phosphorene nanosheets to sustain the oxygen vacancies of BiOBr for excellent photocatalytic nitrogen fixation

Tianqi Wang,[#a] *Rui Zhai,*[#a] *Zhengyi Liu,*[a] *Siyuan Liu,*[a] *Yonghong Cheng*[a] *and Jinying Zhang*[*a]

[a] *State Key Laboratory of Electrical Insulation and Power Equipment, Center of Nanomaterials for Renewable Energy (CNRE), School of Electrical Engineering, Xi'an Jiaotong University, Xi'an, Shaanxi, 710049, PR China*

* *Corresponding author: Email：*jinying.zhang@mail.xjtu.edu.cn

Material synthesis and characterizations

Preparation of VPNS:

The violet phosphorus was produced by a chemical vapor transportation (CVT) method using amorphous red phosphorus as resource and Sn + SnI_4 as transport agents. The as-produced violet phosphorus crystals were ground and simply dispersed in absolute ethanol by ultrasonic tip for 10 h. The suspension was centrifuged and washed three times with absolute ethanol and deionized water. The precipitates were then collected and vacuum-dried at 60°C for 5 h.

Preparation of BiOBr(OVs):

The oxygen vacancy-rich BiOBr(OVs) was synthesized by a solvothermal method. Briefly, 1 mmol $Bi(NO_3)_3 \cdot 5H_2O$ were added into 20 mL ethylene glycol (EG) solution containing stoichiometric amounts of KBr. The mixture was stirred for 1 h at room temperature under ambient conditions, and then poured into a 50 mL Teflon-lined stainless autoclave. The autoclave was heated at 160°C for 12 h under autogenous pressure, and then air cooled to room temperature. The resulting precipitates were collected and washed with deionized water and ethanol to remove the residual ions. The final product was dried at 60°C in air for further use.

In situ FTIR measurement:

In situ diffuse reflectance FTIR spectra were recorded by an INVENIO spectrometer (BRUKER, USA) using a self-designed reaction cell. A thin layer of VPNS-BiOBr(OVs) was pre-deposited on the substrate in the center of the reaction cell. The cell was then purged by Ar, while the temperature was gradually raised to 50°C for 30 minutes to get rid of the absorbed small molecules. A small amount of water vapor was then introduced to pre-adsorb on the surface of samples, followed by a large amount of nitrogen gas create a N_2 atmosphere. Finally, the xenon lamp was turned on and the IR signal was in situ collected by a MCT detector at different reaction time.

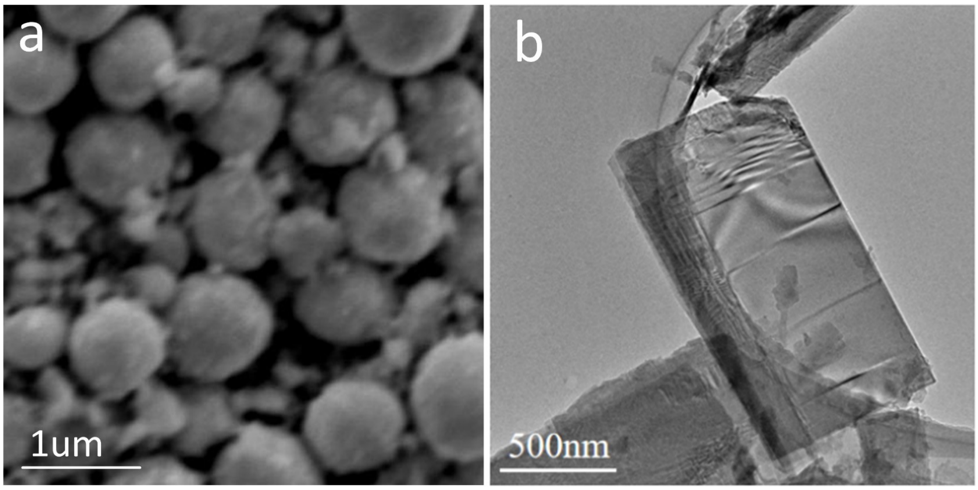

Figure S1. (a) SEM image of pristine BiOBr(OVs) and (b) TEM image of pristine VPNS.

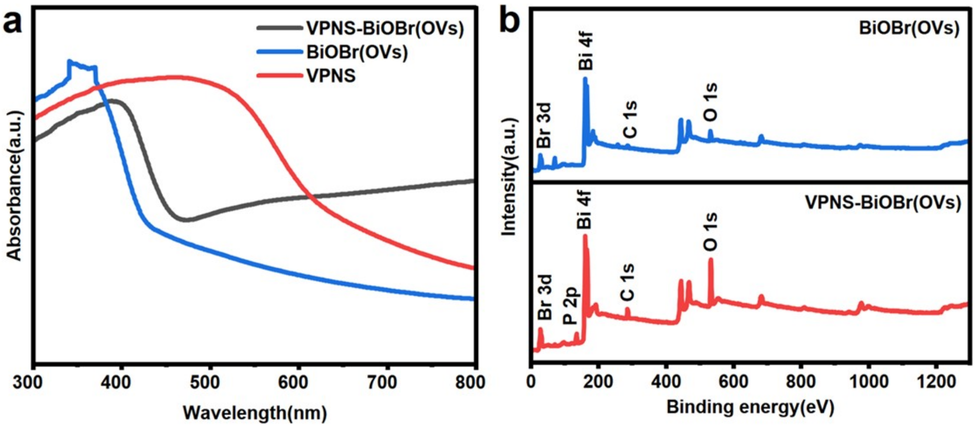

Figure S2. (a) UV-Vis absorption spectra of VPNS, BiOBr(OVs) and VPNS-BiOBr(OVs). (b) Survey XPS spectra of BiOBr(OVs) and VPNS-BiOBr(OVs).

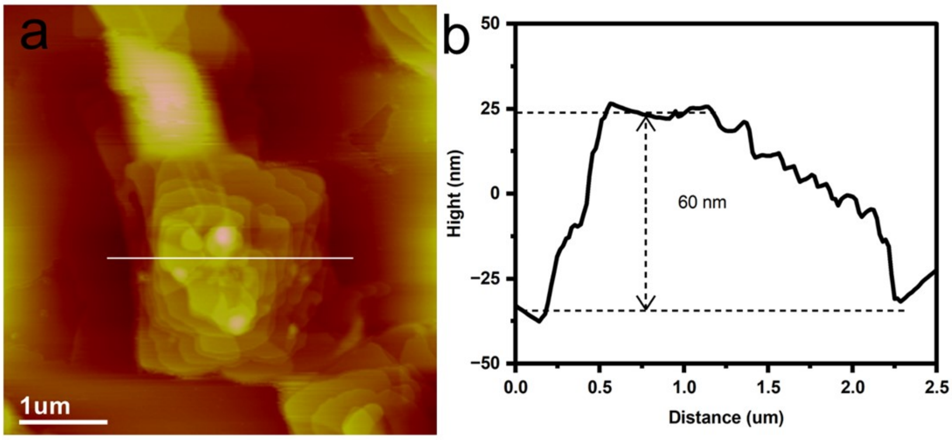

Figure S3. AFM measurement of VPNS. (a) topography of VPNS, (b) corresponding height along the white line in (a).

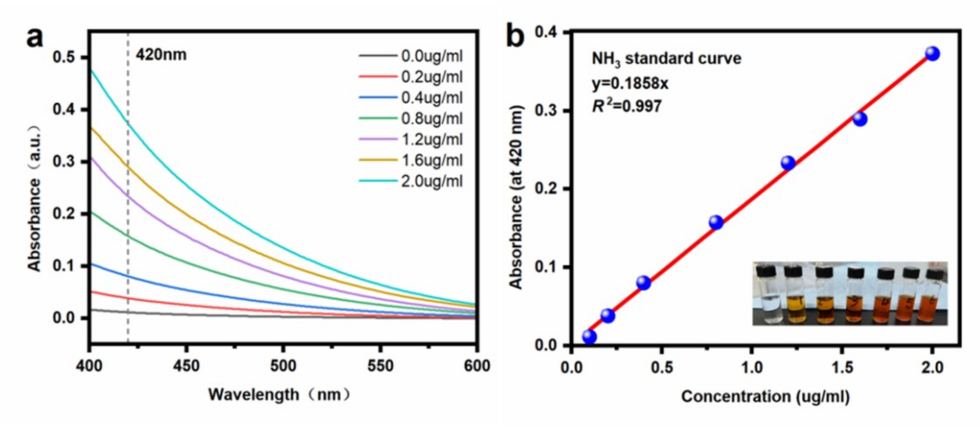

Figure S4. (a) UV-visible spectra of standard ammonia solutions with different concentrations and (b) corresponding calibration curve. The absorbance values of the calibration curve were obtained at a wavelength of 420 nm. The inset of (b) is a photograph of the standard solution after reacting with Nessler's reagent for 20 minutes.

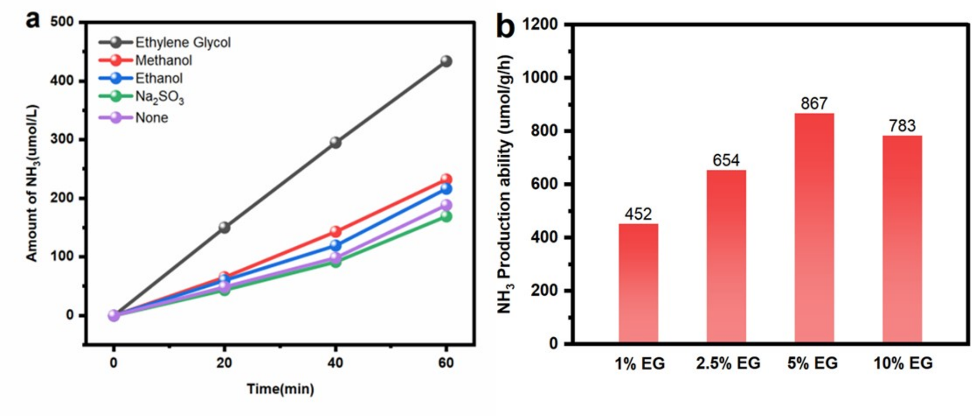

Figure S5. Effect of (a) type and (b) concentration of sacrificial agents on photocatalytic N_2 fixation reactions.

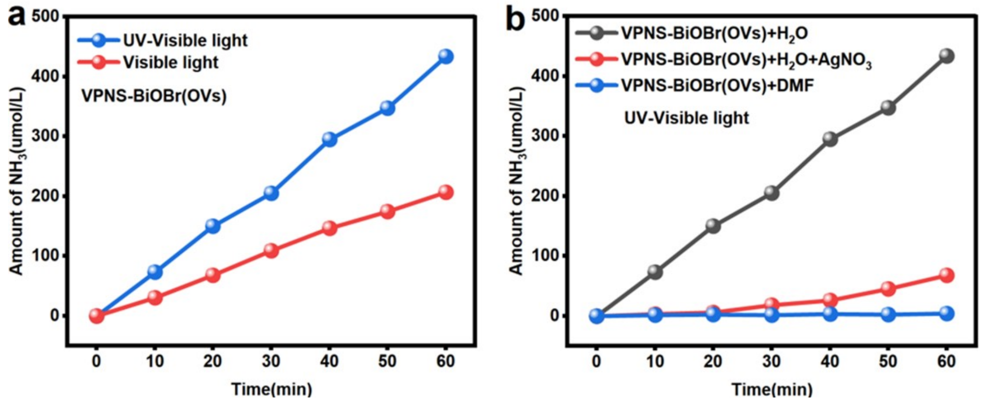

Figure S6. (a) Photocatalytic N_2 fixation performance of VPNS-BiOBr(OVs) under UV-visible light (xenon lamp) and visible light (>420 nm). (b) Photocatalytic N_2 fixation performance of VPNS-BiOBr(OVs) in aprotic solvent (DMF), deionized water, and deionized water with electron scavenger ($AgNO_3$).

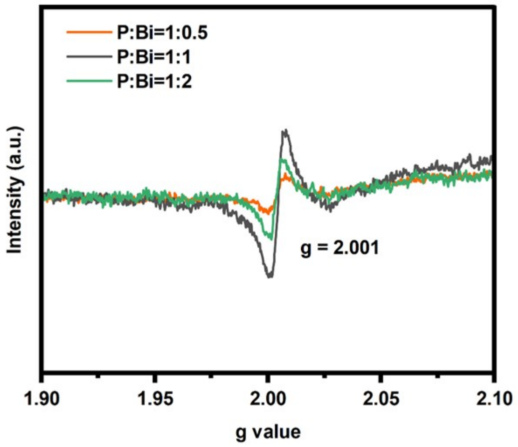

Figure S7. EPR spectra of VPNS-BiOBr(OVs) with different P:Bi molar ratios under the same conditions.

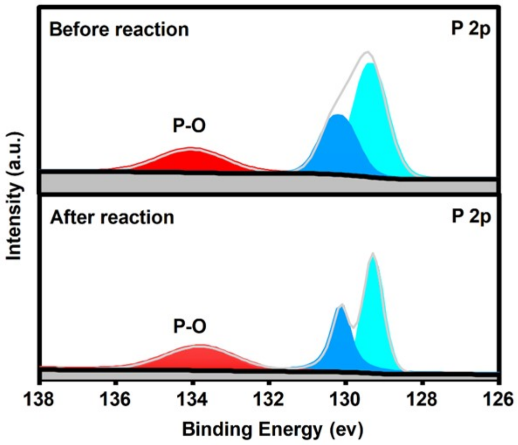

Figure S8. High-resolution P 2p XPS spectra of VPNS-BiOBr(OVs) before and after five reaction cycles.

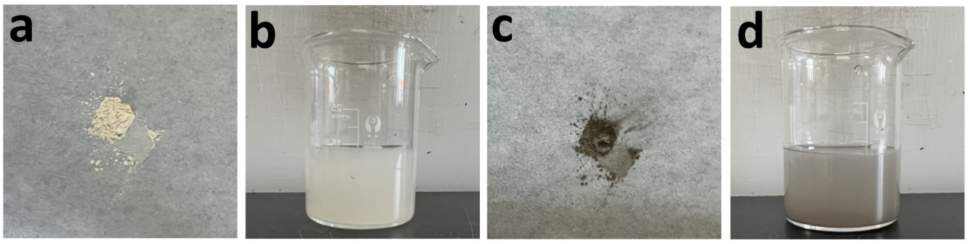

Figure S9. Optical images of BiOBr(OVs) (a) powder and (b) suspension in deionized water before xenon lamp irradiation. Optical images of BiOBr(OVs) (a) powder and (b) suspension in deionized water after xenon lamp irradiation.

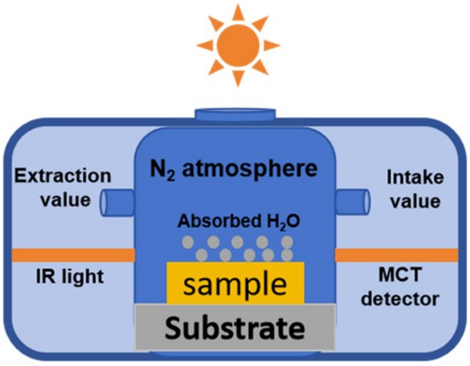

Figure S10. Schematic illustration of the self-designed reaction cell for in situ FTIR spectroscopy.

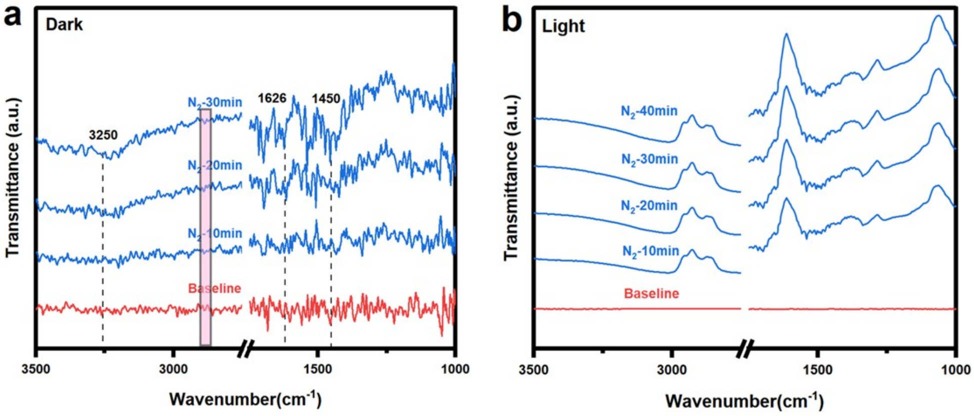

Figure S11. In situ FTIR spectra recorded during the photocatalytic N_2 fixation of BiOBr(OVs) under (a) dark and (b) xenon light irradiation.

Table S1. Comparison of photocatalytic nitrogen fixation performance from different catalysts

Catalyst	Light Source	Co-catalyst	Scavenger	Reaction time (h)	NH_3 yield (umol/g/h) λ>420nm	NH_3 yield (umol/g/h) Uv-Visible	Apparent quantum yield	Highlights	Ref
BiOBr-001-OVs	300W Xenon	No	No	1	104	223.3	0.23% at 420 nm	Oxygen vacancies	1
BiOCl-010-OVs	300W Xenon	No	Methanol	2	92.3	0	4.3% at 254 nm	Oxygen vacancies	2
Fe–$SrMoO_4$	300W Xenon	No	No	1	0	93.1	None	Oxygen vacancies, Fe doping	3
Bi_2MoO_6 /OV-BiOBr	300W Xenon	No	No	1	81	90.7	None	Oxygen vacancies, Heterojunctions	4
Mo-doped Bi_5O_7Br-OVs	300W Xenon	No	No	2	122.9	0	None	Switchable Oxygen vacancies, Mo dopants	5
Fe/BiOCl(OVs) NSs	300W Xenon	No	No	1.5	0	1022	1.8% at 420 nm	Oxygen vacancies, Fe doping	6
BiO quantum dots	500W Xenon	No	No	1	0	1226	None	quantum dots	7
BPNSs/CdS	300W Xenon	No	Methanol	4	240.2	0	None	Metal-free Cocatalyst	8
BPCNS	500W Xenon	No	Methanol	4	577.5	0	None	Metal-free Cocatalyst, C-P bonds	9
Ga_2O_3-DBD /g-C_3N_4	500W Xenon	No	Methanol	5	0	281.25	None	Heterojunctions, Z-scheme	10
$W_{18}O_{49}$/g-C_3N_4	300W Xenon, & 200W IR	No	Ethanol	4	0	145	None	Heterojunctions, Z-scheme	11
TiO_2@C/g-C_3N_4	300W Xenon	No	Methanol	2	250.6	0	0.14% at 420 nm	Heterojunctions	12
TiO_2-OVs	300W Xenon	No	Methanol	1	0	324.86	1.1% at 365 nm	Tunable defect structure, Oxygen vacancies	13
TiO_2/$ZnFe_2O_4$	250W Xenon	No	Methanol	1.6	0	88.8	None	Oxygen vacancies, Z-scheme	14

Au/TiO$_2$-OVs	300W Xenon	Au	Methanol	1.6	78.6	0	0.82% at 550 nm	Oxygen vacancies,	[15]
Cu–TiO$_2$-OVs	300W Xenon	No	No	3	0	78.9	0.08% at 600 nm	Oxygen vacancies, Cu doping	[16]
VPNS-BiOBr(OVs) (This work)	300W Xenon 320～780 nm	No	Ethylene Glycol	1	412	867	1.7% at 380 nm	Oxygen vacancies, Heterojunctions	

Reference

1. H. Li, J. Shang, Z. Ai and L. Zhang, *Journal of the American Chemical Society*, 2015, **137**, 6393-6399.
2. H. Li, J. Shang, J. Shi, K. Zhao and L. Zhang, *Nanoscale*, 2016, **8**, 1986-1993.
3. J. Luo, X. Bai, Q. Li, X. Yu, C. Li, Z. Wang, W. Wu, Y. Liang, Z. Zhao and H. Liu, *Nano Energy*, 2019, **66**, 104187.
4. X. Xue, R. Chen, C. Yan, Y. Hu, W. Zhang, S. Yang, L. Ma, G. Zhu and Z. Jin, *Nanoscale*, 2019, **11**, 10439-10445.
5. X. Chen, M.-Y. Qi, Y.-H. Li, Z.-R. Tang and Y.-J. Xu, *Chinese Journal of Catalysis*, 2021, **42**, 2020-2026.
6. N. Zhang, L. Li, Q. Shao, T. Zhu, X. Huang and X. Xiao, *ACS Applied Energy Materials*, 2019, **2**, 8394-8398.
7. S. Sun, Q. An, W. Wang, L. Zhang, J. Liu and W. A. Goddard Iii, *Journal of Materials Chemistry A*, 2017, **5**, 201-209.
8. Z.-K. Shen, Y.-J. Yuan, P. Wang, W. Bai, L. Pei, S. Wu, Z.-T. Yu and Z. Zou, *ACS applied materials & interfaces*, 2020, **12**, 17343-17352.
9. P. Qiu, C. Xu, N. Zhou, H. Chen and F. Jiang, *Applied catalysis B: environmental*, 2018, **221**, 27-35.
10. S. Cao, N. Zhou, F. Gao, H. Chen and F. Jiang, *Applied Catalysis B: Environmental*, 2017, **218**, 600-610.
11. H. Liang, H. Zou and S. Hu, *New Journal of Chemistry*, 2017, **41**, 8920-8926.
12. Q. Liu, L. Ai and J. Jiang, *Journal of Materials Chemistry A*, 2018, **6**, 4102-4110.
13. G. Zhang, X. Yang, C. He, P. Zhang and H. Mi, *Journal of Materials Chemistry A*, 2020, **8**, 334-341.
14. X. Rong, H. Chen, J. Rong, X. Zhang, J. Wei, S. Liu, X. Zhou, J. Xu, F. Qiu and Z. Wu, *Chemical Engineering Journal*, 2019, **371**, 286-293.
15. J. Yang, Y. Guo, R. Jiang, F. Qin, H. Zhang, W. Lu, J. Wang and J. C. Yu, *Journal of the American Chemical Society*, 2018, **140**, 8497-8508.
16. Y. Zhao, Y. Zhao, R. Shi, B. Wang, G. I. N. Waterhouse, L. Z. Wu, C. H. Tung and T. Zhang, *Advanced Materials*, 2019, **31**.